Evidence of massive Dirac fermions in the kagome nodal-line semimetal $Ni_3In_2S_2$ as revealed by high magnetic field studies

Sangjin Kim,[1] Kwang-Tak Kim,[1] Min Hyuk Choi,[2] Hyungwon Nam,[3] Jun Seong Lee,[2] Joonyoung Choi,[4] Yeahan Sur,[1] Kiwan Nam,[1] Hyunju Hwang,[1] Jungwon Choi,[1] Eun Sang Choi,[5] Woun Kang,[6] Youn Jung Jo,[4] Jun Sung Kim,[2] Soonjae Moon,[3] and Kee Hoon Kim[1,7,*]

[1]*Department of Physics and Astronomy, Seoul National University, Seoul 08826, Republic of Korea*
[2]*Department of Physics, Pohang University of Science and Technology, Pohang 37673, Republic of Korea*
[3]*Department of Physics, Hanyang University, Seoul 04763, Republic of Korea*
[4]*Department of Physics, Kyungpook National University, Daegu 41566, Republic of Korea*
[5]*National High Magnetic Field Laboratory, Florida State University, Tallahassee, Florida 32310, USA*
[6]*Department of Physics, Ewha Womans University, Seoul 03760, Republic of Korea*
[7]*Institute of Applied Physics, Department of Physics and Astronomy, Seoul National University, Seoul 08826, Republic of Korea*

(Received 29 January 2025; revised 21 June 2025; accepted 1 July 2025; published 24 July 2025)

We present evidence of nontrivial topology in the kagome semimetal $Ni_3In_2S_2$ from quantum oscillation experiments at high magnetic fields up to 31 T and theoretical investigations by first-principles calculations. Angle-dependent de Haas–van Alphen oscillations reveal the presence of quasi-two-dimensional hole and three-dimensional electron pockets, consistent with first-principles calculations, along with signatures of magnetic breakdown across these pockets. In particular, we find that the smallest cyclotron orbit, $F_\alpha \approx 10$ T, enclosing theoretically predicted endless Dirac nodal lines, has a relatively low effective mass of $0.183m_0$ and a Berry phase close to π. Furthermore, this orbit has a high quantum mobility of 0.88 $m^2\ V^{-1}\ S^{-1}$, an order of magnitude larger than that of the heavier charge carriers. Infrared spectroscopy reveals linearly increasing optical conductivity with photon energy above 45 meV. These experimental results, as confirmed by first-principles calculations, support that massive Dirac fermions, formed by a small gap opening due to spin-orbit coupling, possess nontrivial topology and can contribute considerably to electrical transport. We also observe linear magnetoresistance above 12.7 T, which can be attributed to the quantum magnetoresistance of the Dirac fermions concentrated on the zeroth Landau level.

DOI: 10.1103/6jzx-mdjv

I. INTRODUCTION

Kagome materials have gained much interest due to the correlated electronic structures from their unique (quasi-) two-dimensional (2D) geometry [1], capable of hosting van Hove singularities, flat bands, and Dirac fermions in the vicinity of the Fermi level [2]. All these features in the electronic structures, partly related to destructive quantum phase interference of hopping electrons on the corner-sharing triangular lattice, have led to exotic physical phenomena as well as topologically nontrivial behaviors such as double-dome superconductivity [3–5], Kondo coupling [6,7], and intrinsic Berry curvature [8,9].

Among these interesting physical phenomena, effects of nontrivial topology have been relatively less explored. Indeed, not all the kagome metals can be unambiguously determined to be topologically nontrivial. For identifying the kagome metals exhibiting the nontrivial topology, it is prerequisite to consider several conditions/challenges. First, the proximity of the nontrivial bands to the Fermi level is crucial. For example, nodal lines are expected in various materials having centrosymmetric space groups [10], but their mere presence does not guarantee contribution to the Fermi surface. In many cases, additional fine-tuning of the Fermi level through carrier doping is necessary to observe phenomena arising from nontrivial bands [11]. Second, identifying exact origins of the observed phenomena is also important. CsV_3Sb_5, for instance, exhibits charge-density wave orders, nematicity, anomalous Hall effect, and superconductivity [12], all stemming from its complex Fermi-surface shape. However, its proximity to two van Hove singularities and three nodal lines, combined with the Brillouin-zone folding [13], makes it difficult to pinpoint a distinct origin for each phenomenon.

Finally, it is common to have multiple scenarios for explaining transport data, making it often ambiguous whether the experimental results can be attributed to nontrivial topology. In a recent report on $Ni_3In_2S_2$, Zhang *et al.* [14] argued that the nonsaturating giant magnetoresistance (MR), one of the highest among kagome materials, is induced by Dirac nodal lines based on their first-principles calculations. In contrast, Fang *et al.* [15] interpreted their Hall transport data to suggest that the giant MR primarily arises from the conventional charge-carrier compensation. Although both groups used electrical transport data, angle-resolved photoemission spectroscopy, and first-principles calculations, their conclusions diverged, highlighting the need for further studies to clarify the role of band topology of $Ni_3In_2S_2$. In this

*Contact author: optopia@snu.ac.kr

context, Zhang *et al.* [16] recently measured quantum oscillations and proposed that a high carrier mobility of a hole pocket, combined with the linear MR at high fields, could explain the extreme MR observed up to 14 T.

In this article, we investigate the Fermi surface of the kagome semimetal $Ni_3In_2S_2$ by the measurements of quantum oscillations and optical conductivity, complemented by first-principles calculations. Torque magnetometry was performed under high magnetic fields up to 31 T and at low temperature down to 0.44 K revealing clear de Haas–van Alphen (dHvA) oscillations from multiple Landau levels crossing the Fermi level, along with signatures of reconstructed cyclotron orbits due to magnetic breakdown. The oscillation frequencies observed in the dHvA signals align well with our density-functional theory (DFT) calculations. Given the presence of the Dirac pockets enclosing the nodal lines [14], we have further conducted vibrating sample magnetometer (VSM) measurements to confirm the small effective mass and nonzero Berry phase. Additionally, optical conductivity measurements were used to investigate the effect of spin-orbit coupling (SOC) and nodal-line characteristics of the massive Dirac bands.

II. METHODS

$Ni_3In_2S_2$ single crystals were grown using the self-flux method [17]. A stoichiometric mixture of Ni powders (99.9%, Alfa Aesar), In shots (99.9995%, Alfa Aesar), and S powders (99.999%, Alfa Aesar) was placed in an alumina crucible, vacuum sealed in a quartz tube and heated up to 900 °C for 72 h. The resultant material was cut into single-crystalline pieces for characterizations using x-ray diffraction (XRD), electrical transport, magnetization, and infrared spectroscopy. XRD patterns were collected at room temperature using a PANalytical Empyrean diffractometer with Cu Kα_1 radiation. Resistivity was measured in a Physical Properties Measurement System (PPMS, Quantum Design) using the standard four-probe method. Magnetic moment measurements were performed with the PPMS-VSM option at a field-sweep rate of 0.3 T/min. Optical conductivity was measured via Fourier transform infrared spectroscopy (VERTEX 70 v, Bruker) and spectroscopic ellipsometry (M-2000, J.A. Woollam).

High-field measurements were performed at the National High Magnetic Field Laboratory, Tallahassee, FL, using a water-cooled resistive magnet with applied field up to 31.46 T, equipped with a ^{3}He cryostat. A piezoresistive cantilever (PRC120, Seiko) was installed on a sample platform to hold a 100×50 μm^2 $Ni_3In_2S_2$ single-crystal piece with Apiezon N grease. A Wheatstone bridge was constructed, consisting of a reference resistor located at the sample space and two variable resistors at room temperature to amplify the balanced signal from the cantilever. The sample was rotated in a magnetic field as the angle θ was varied from $-15°$ to 85° in 5° steps, where $\theta = 0°$ (90°) corresponds to $\boldsymbol{H}||\boldsymbol{c}(\boldsymbol{a})$. The field was swept at a rate of 2 T/min.

To calculate the electronic structures, first-principles calculations based on DFT [18] were performed using the QUANTUM ESPRESSO software package [19]. Pseudopotentials based on the projector augmented-wave method [20] were employed, along with the generalized gradient approximation exchange-correlation functional in the Perdew-Burke-Ernzerhof scheme [21]. Self-consistent calculations were converged with a plane-wave cutoff energy of 1020 eV and a $17 \times 17 \times 17$ k mesh. The FERMISURFER application [22] was used to plot the calculated three-dimensional (3D) Fermi surfaces using a $61 \times 61 \times 61$ k mesh.

III. RESULTS AND DISCUSSION

Figure 1(a) shows the primitive unit cell of $Ni_3In_2S_2$ in the rhombohedral structure with space group R-3m, and Fig. 1(b) shows the ab plane composed of Ni and S ions in the conventional hexagonal structure, where Ni forms a kagome network. An optical image of a $Ni_3In_2S_2$ single crystal is shown in the inset of Fig. 1(c), where the shiny flat surface is identified as the (00l) plane based on XRD patterns. Figure 1(d) displays the field-dependent longitudinal resistivity, showing large MR without saturation up to 31 T. The inset of Fig. 1(d) shows the temperature dependence of resistivity. At $\mu_0 H = 0$ T, the resistivity increases with temperature, exhibiting metallic behavior, while at 10, 20, and 30 T it decreases, becoming insulator-like with similar spacing, reflecting the linearity in MR. Figure 1(e) shows the electronic band structure from DFT calculations with and without SOC. Two electron bands and a hole band crossing the Fermi level can be seen, with Dirac nodes near B and B1 points. Small SOC-induced gaps can be found at the Dirac nodes, which will be discussed in detail later. Signatures of a nodal loop formed from two electron bands can be seen in the ΓL line, consistent with the previous reports by Zhang *et al.* [14]. Figure 1(f) shows the Fermi surface derived from the DFT calculations. Around the inversion center Γ, the electron bands form closed pockets (red and green), while the hole band forms quasi-2D pockets (blue). The structure holds threefold rotational symmetry around the ΓZ axis and mirror symmetry along the ZLΓ plane, revealing the chirality of hole pockets around B/B1 points similar to graphene's [23–25]. It is worth noting that the B and mirrored B1 are the identical points considering the repeated zone scheme (Fig. S4(c) [26]) in the vicinity of theoretically predicted endless nodal lines with a nonzero Berry phase [14].

To explore the fermiology of $Ni_3In_2S_2$ in detail, we measured torque signals under high magnetic fields up to 31 T. Figure 2(a) shows the field dependence of the torque at fixed temperatures ranging from 1.5 to 11 K. The sample has been tilted at a small angle of $\theta = -15°$, as illustrated in the inset of Fig. 2(a), to enhance the signal and modulate separations between orbits in momentum space. Clear dHvA oscillations are observed above 10 T, which become more conspicuous in the background-subtracted oscillations in the inverse field plot shown in Fig. 2(b). The oscillations reveal the presence of multiple orbits, with their amplitudes gradually diminishing at higher temperatures.

Figure 2(c) shows the fast Fourier transformation (FFT) spectra of the data shown in Fig. 2(b). We could identify various frequencies, including all five expected fundamental orbits ($F_\alpha \approx 14$ T, $F_\beta \approx 628$ T, $F_\gamma \approx 749$ T, $F_\delta \approx 1195$ T, and $F_\varepsilon \approx 2885$ T) that follow the Onsager relation [27], $F = \frac{\hbar}{2e} k_F^2$, where $\hbar$, e, and k_F are reduced Planck constant, elementary charge, and Fermi wave vector, respectively. The FFT results are in agreement with the DFT calculations and

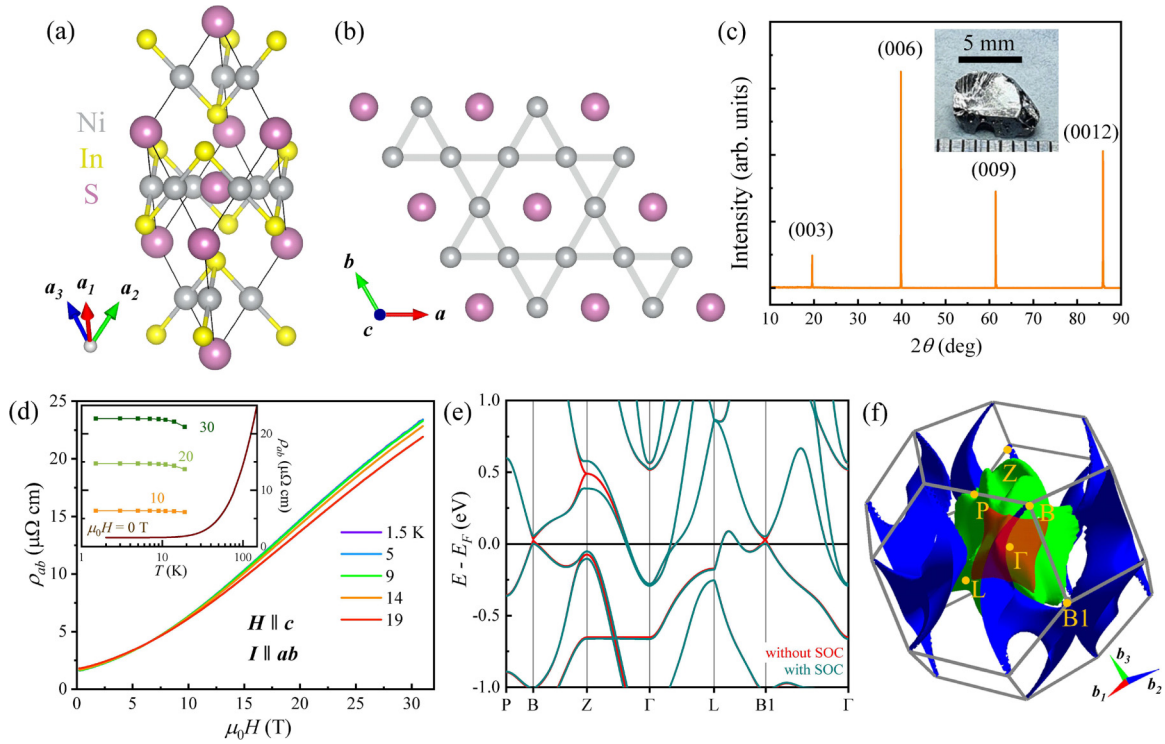

FIG. 1. (a) A primitive cell of $Ni_3In_2S_2$ in the rhombohedral structure. For DFT calculations, the primitive cell has been used, while other descriptions are based on the hexagonal structure. (b) The *ab* plane of $Ni_3In_2S_2$ in the hexagonal kagome structure. (c) XRD patterns of a $Ni_3In_2S_2$ single crystal. The inset shows an optical image of a crystal piece, reaching a typical length of 5 mm. (d) Longitudinal resistivity of $Ni_3In_2S_2$ measured by sweeping magnetic field up to 31 T. The inset is comparison of longitudinal resistivity at 0, 10, 20, and 30 T. (e) Band calculation results with and without SOC. (f) The first Brillouin zone of $Ni_3In_2S_2$. Red and green colors represent electron pockets around Γ, and blue refers to a hole pocket. For visualization, the red pocket, which should be located inside the green, is plotted outside, being partially transparent.

previous quantum oscillation measurements [16]. In addition to the fundamental orbits, we also observed their subpeaks, second harmonics (e.g., 2β), and features indicative of magnetic breakdown. Subpeaks could arise from a slight in-plane misalignment of the sample, which breaks the mirror symmetry of the Fermi surface at nonzero θ and lifts the degeneracies of the extremal orbits. Harmonics are integer multiples of fundamental orbits, and typically exhibit reduced oscillation intensities [27]. Tunneling orbits are denoted as $\delta + t$, $\varepsilon - \gamma$, and $s + t$. These are observed exclusively in the high-field regime above 14 T (Fig. S3 [26]) and will be discussed in more detail later.

Amplitude of quantum oscillations can be described using the Lifshitz-Kosevich (LK) formula [27]:

$$\Delta\tau(T,\ H) \propto H^{3/2} \frac{\lambda(T/H)}{\sinh[\lambda(T/H)]} e^{-\lambda(T_D/H)}, \qquad (1)$$

where $\lambda(T/H) = \frac{2\pi^2 k_B m^*}{\hbar e} \frac{T}{\mu_0 H}$, with T_D, k_B, and m^* representing Dingle temperature, Boltzmann constant, and effective mass of the carriers, respectively. The LK formula describes the attenuation of oscillation amplitudes with increasing temperature and decreasing magnetic field. Figure 2(d) displays the effective masses of the carriers on cyclotron orbits determined using the LK formula with the average field, $\langle H \rangle = 2H_{\rm low} H_{\rm high}/(H_{\rm low} + H_{\rm high})$, within the field window of 13.3 to 31 T. The obtained effective masses are $m^*_\beta = (0.625 \pm 0.008)m_0$, $m^*_\gamma = (0.794 \pm 0.021)m_0$, $m^*_\delta = (1.06 \pm 0.08)m_0$, and $m^*_\varepsilon = (0.98 \pm 0.11)m_0$, where m_0 is the free-electron mass. Orbit α, which exhibits barely one period of oscillation at $\mu_0 H > 10$ T, reflecting its small Fermi-surface intersection, will be examined further using lower-temperature torque and VSM data for more detailed analysis.

To obtain theoretical insights and visualize the extremal cyclotron orbits of $Ni_3In_2S_2$, we conducted DFT calculations and plotted the 2D cross sections of the 3D Brillouin zone. Figure 3(a) shows the fundamental orbits under $\boldsymbol{H} \parallel \boldsymbol{c}$; orbits α, β, and γ from the hole band are depicted in blue, while orbit δ (ε) from the electron 1 (2) band is shown in red (green). Note that the two electron bands form nodelike features around the Γ point, and the electron 2 and hole bands are closely positioned along the ΓX line. These small separations in momentum space are essential conditions for magnetic breakdown, where charge carriers tunnel into another band under sufficiently high magnetic fields [27,28]. Figure 3(b) illustrates an example of the tunneling orbit $\varepsilon + 3t$, which includes three triangular bounded sections, t, around δ. Considering the rotating directions of the carriers, section t itself cannot form a closed orbit, but it is the path difference between orbits δ and ε, making it a crucial part in magnetic breakdown; carriers on orbit δ can tunnel into ε, and vice versa, gaining or losing section t, corresponding to $(F_\varepsilon - F_\delta)/6$ in FFT frequencies. As a result, several frequencies with similar spacings are expected; in fact, between

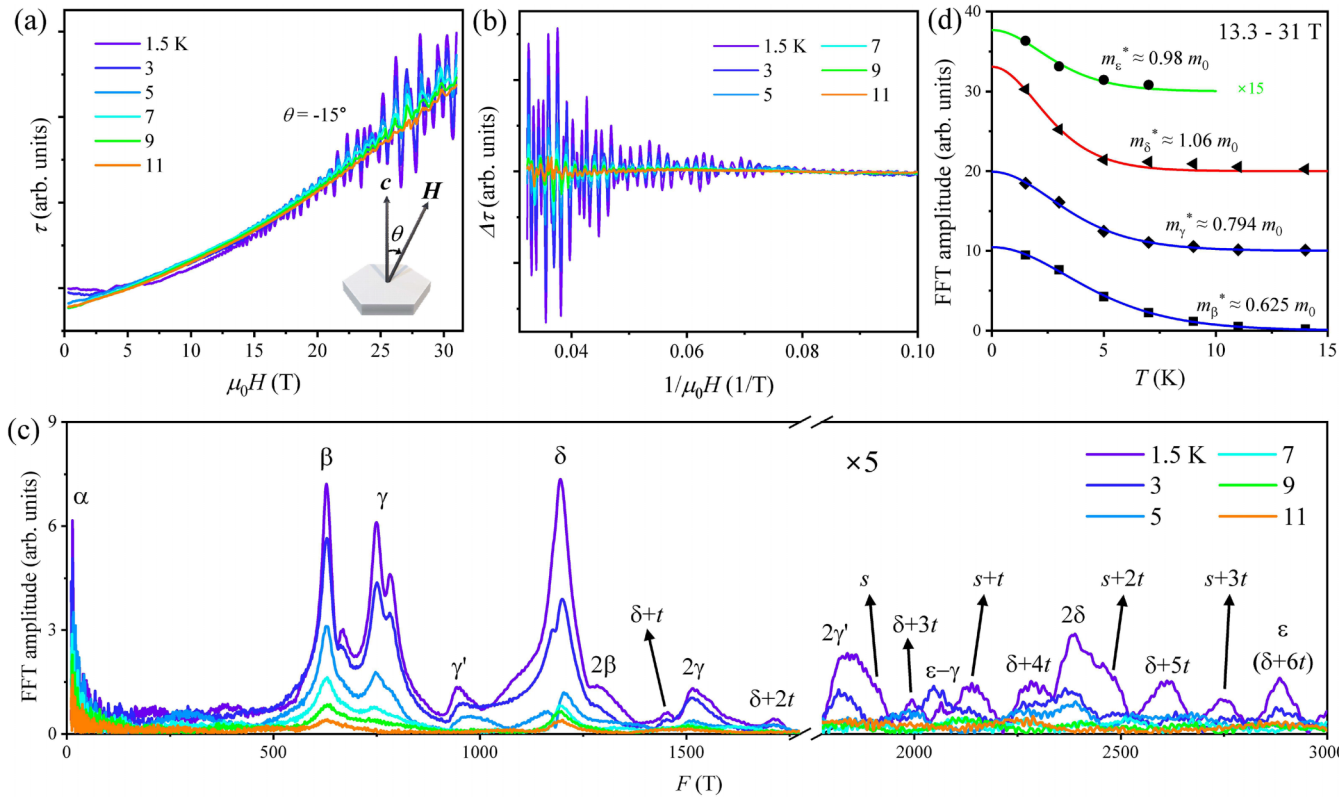

FIG. 2. (a) Magnetic field dependence of torque signals under fixed temperatures. The inset is a schematic of the magnetic field direction with respect to the single-crystalline $Ni_3In_2S_2$ sample on the cantilever (Fig. S1 [26]). (b) Inverse field dependence of background-subtracted torque data by polynomial fitting, leaving dHvA oscillations. (c) FFT spectra of the oscillations in (b). Frequency peaks above 1775 T are fivefold enhanced to clearly visualize the low-intensity orbit frequencies. (d) Effective mass of orbits β, γ, δ, and ε obtained from oscillations in 13.3–31 T window. The orbit ε curve is 15-fold enhanced and each curve is linearly shifted for visualization.

F_δ and F_ε, five similarly spaced tunneling orbits are observed, with each increasing by $(F_\varepsilon - F_\delta)/6$.

In addition, due to the proximity of the hole orbit γ to the electron orbit ε, Klein tunneling, which allows conversion of an electron (a hole) into a hole (an electron) by traversing a potential barrier, can occur, generating tunneling orbits encompassing the electron and hole orbits [29]. Under these conditions, the orbits γ, δ, and ε may all contribute to magnetic breakdown, complicating the assignment of specific orbits but still likely resulting in a similar spacing of $(F_\varepsilon - F_\delta)/6$. Tunneling orbits $s + zt$, where s represents an arbitrary orbit and z is an integer [Fig. 2(c)], are possibly the result of three-band interactions as suggested in Fig. S5 [26]. Notably, the complex appearance of these tunneling orbits resembles those observed in other nodal-line semimetals, such as (Zr,Hf)Si(S,Se,Te) [30–33], indicating that $Ni_3In_2S_2$ may be a candidate for exploring the unique properties associated with nodal loops [30,34].

Figure 3(c) presents the angle dependence of FFT amplitudes of dHvA oscillations measured at 0.44 K using torque magnetometry, ranging from $\theta = -15\,^\circ$ to $85\,^\circ$ on a linear scale. Between F_δ (pale red) and F_ε (pale green), a frequency $F_{\delta+3t} = (F_\delta + F_\varepsilon)/2$ (pale dashed yellow), corresponding to a tunneling orbit $\delta + 3t$, is identified, illustrating the angle dependence of field-induced tunneling for $\theta \leqslant 65^\circ$. For $\theta \geqslant 70^\circ$, tunneling orbits disappear, and interestingly, the second-harmonic frequency of δ, $F_{2\delta} = 2F_\delta$ (pale dashed red), becomes more prominent. The absence of tunneling at large θ can be attributed to changes in the 2D intersections of the Fermi surface, which results in larger separations between the electron pockets. Figure 3(d) shows the angle dependence of FFT frequencies for orbits α, β, γ, δ, ε, and their subpeaks, compared with DFT simulations in Fig. 3(e). Overall, the two datasets qualitatively agree, although minor differences may arise from imperfect sample alignment due to its small size. The relatively simpler morphologies of the two electron bands make them less sensitive to slight misalignment, leading to good agreement to simulations. In contrast, the hole band, with its more complex shape, sixfold degenerate orbits at $\theta = 0\,^\circ$ are expected to split into twofold and fourfold degeneracies at nonzero θ. These degeneracies may be further lifted in real experiments by finite offsets in the azimuthal angle. Although unexpected subpeaks from hole pockets were observed at low θ, it is noteworthy that the sharp increase in F_β around $\theta = 55\,^\circ$ in the DFT simulations [Fig. 3(e)] aligns well with experimental findings [pale-blue curve in Fig. 3(c)], showing the quasi-2D nature of the hole band (Fig. S6 [26]).

To examine the orbit α in detail, we performed VSM measurements up to 9 T and compared it with sub-Kelvin high-field torque results. Figure 4(a) shows dHvA oscillations of a $Ni_3In_2S_2$ single crystal (28.9 mg) with $\boldsymbol{H} \parallel \boldsymbol{c}$. Four peaks, $F_\alpha \approx 10$ T, $F_\beta \approx 592$ T, $F_\gamma \approx 661$ T, and $F_\delta \approx 1293$ T, were detected from the FFT of dHvA oscillations, with no peaks visible above 1500 T. The F_α oscillations exhibit notable

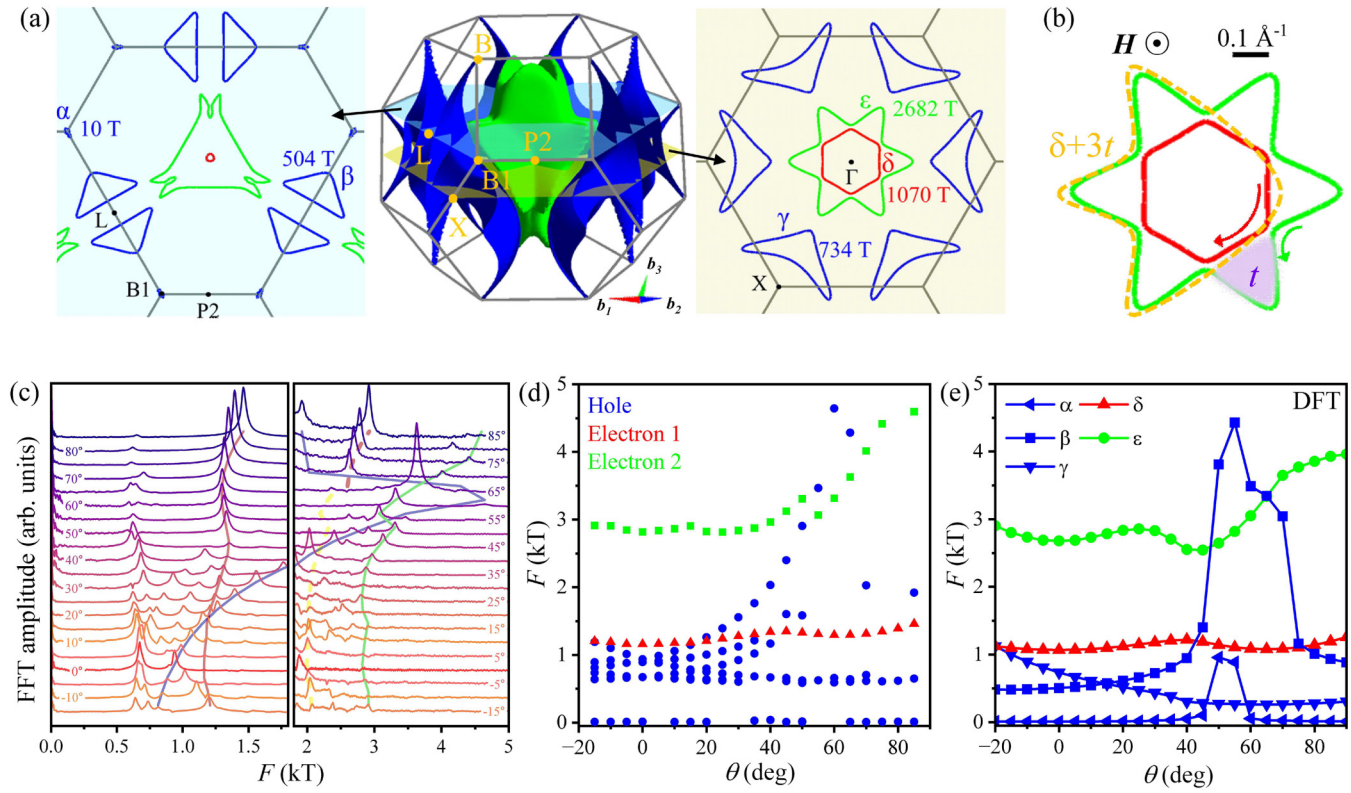

FIG. 3. (a) Cross sections of the two Fermi surfaces exhibiting extremal orbits of α, β (left) and γ, δ, and ε (right) under $\boldsymbol{H} \parallel \boldsymbol{c}$, and their locations in the first Brillouin zone. The dHvA frequency is also represented in each extremal orbit. (b) Schematics of the tunneling orbit $\delta + 3t$ (dashed yellow line) and the bounded section t (hatched violet region). Orbit $\delta + 3t$ includes three t sections around orbit δ. Arrows indicate the possible route of charge carriers in crystal momentum space. (c) Angle-dependent FFT spectra at 0.44 K, vertically offset and individually scaled for clarity, from $\theta = -15°$ to 85°. Pale blue, red, and green lines, along with pale dashed red and yellow lines, serve as guides to the eye indicating the orbits assigned as γ, δ, ε, 2δ, and $\delta + 3t$, respectively. (d) Angle dependence of dHvA frequencies replotted from (c) after second-harmonic and tunneling orbit frequencies above 1 kT being removed. (e) Angle dependence of fundamental orbit frequencies as predicted by DFT simulations.

intensity that decrease with increasing temperature, as shown in Fig. 4(b), which is derived from local minima at $\mu_0 H \approx 4.7$ T in the bandpass-filtered ΔM. The effective mass of carriers on orbit α, $m^*_\alpha = (0.183 \pm 0.012)m_0$, is significantly smaller than that of all the other orbits (Table I) reflecting the linear Dirac dispersion near B/B1 [Fig. 1(g)].

Given that F_α is as small as 10 T, the magnetic field required to observe the first Landau level crossing the Fermi level is likely to be below 31 T. Thus, assigning the Landau level index n is crucial for confirming whether the quantum limit has been reached for the orbit α. The quantized Landau level dispersion for massive Dirac bands can be

TABLE I. Physical parameters related to charge carriers on cyclotron orbits; quantum oscillation frequency (F), Fermi wave vector (k_F), effective mass (m^*), Dingle temperature (T_D), quantum scattering time (τ_s), and quantum mobility (μ), obtained from dHvA oscillations of $Ni_3In_2S_2$ using torque magnetometry at $\theta = -15°$ and VSM measurements with $\boldsymbol{H} \parallel \boldsymbol{c}$. The datasets for each orbit marked with the symbol † (second column) represent parameters extracted from the VSM data. All parameters except for the effective mass were obtained at 1.5 K for the torque and 2 K for the VSM results.

Orbit	F (T)	k_F (Å^{-1})	m^*/m_0	T_D (K)	τ_s (ps)	μ (m^2 V^{-1} S^{-1})
α	10.0(1)†	0.0174(1)	0.183(12)	1.32(45)	0.92(31)	0.88(30)
β	592.1(3)†	0.1341(3)	0.841(28)	3.10(19)	0.392(24)	0.0820(57)
	628.3(1)	0.1382(1)	0.625(8)	5.91(23)	0.206(8)	0.0580(24)
γ	661(1)†	0.1417(1)	1.11(15)	2.16(31)	0.563(81)	0.089(18)
	748.9(1)	0.1509(1)	0.794(21)	4.17(23)	0.292(16)	0.0647(39)
δ	1292.8(3)†	0.1982(3)	0.649(46)	6.84(62)	0.178(16)	0.0482(55)
	1194.9(1)	0.1905(1)	1.06(8)	5.94(48)	0.205(17)	0.0340(38)
ε	2885.4(1)	0.2961(1)	0.98(11)	20.5(24)	0.0593(69)	0.0106(17)

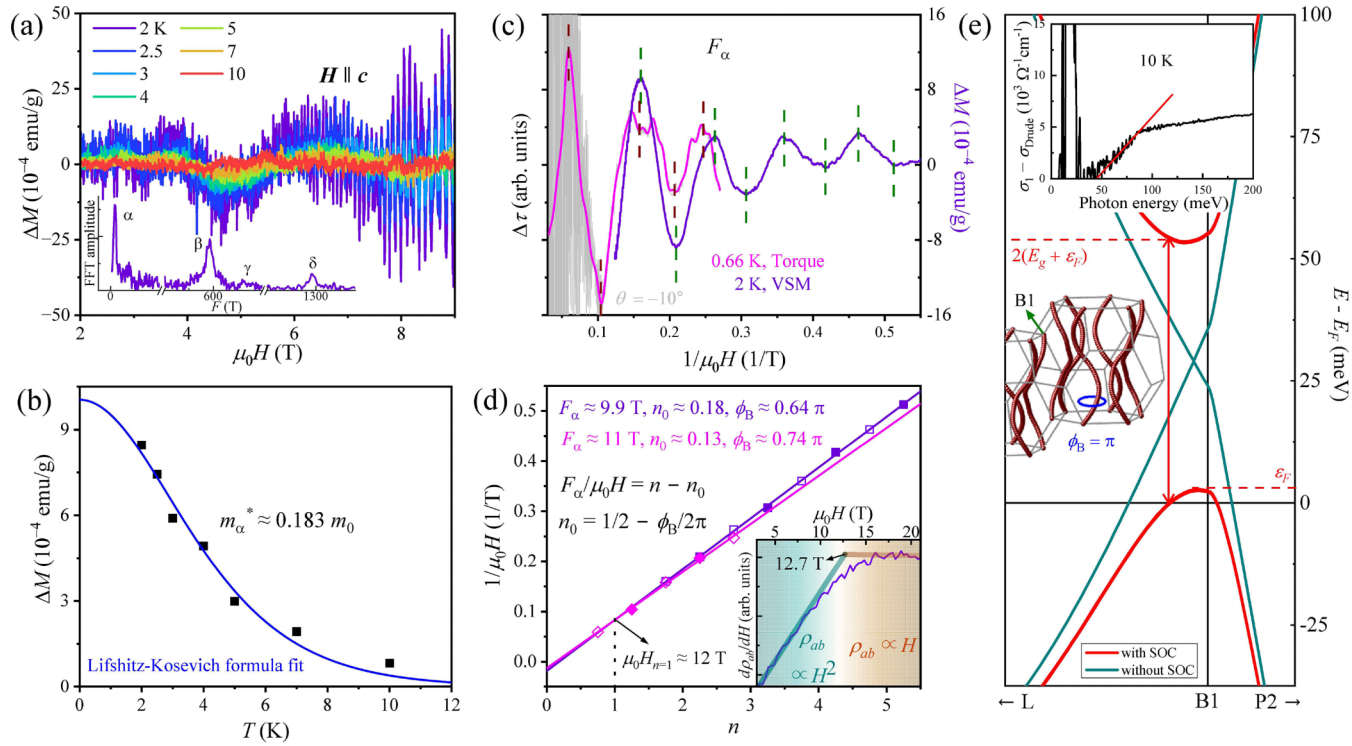

FIG. 4. (a) Field dependence of polynomial background-subtracted magnetic moment measured with VSM. The inset shows the FFT spectrum of the 2 K oscillations in inverse field, demonstrating the presence of fundamental orbits α, β, γ, and δ. (b) Effective mass of orbit α extracted from oscillation minima at the Landau level index $n = 2.25$ ($\mu_0 H \approx 4.7$ T), which was obtained from the bandpass-filtered data (5–15 T) of (a) in inverse field. (c) F_α oscillations in inverse field. The gray curve represents background-subtracted magnetic torque at $T = 0.66$ K and $\theta = -10^\circ$ in the 3.7–31.46 T window, and the magenta curve shows the low-pass filtered result. The violet curve is the adjacent-averaging smoothed 2 K data in (a). Dashed lines indicate the positions of local maxima and minima. (d) Landau fan diagram of F_α oscillations in (c). Empty (filled) symbols represent oscillation maxima (minima). Both linear extrapolations show Berry phase close to π. The inset is the first derivative of longitudinal resistivity under magnetic field at 1.5 K. Thicker lines represent linear fits at 2–7 T and 16–20 T. (e) Band structure of $Ni_3In_2S_2$ near B1. Without SOC, a Dirac node is located between L and B1 with linear dispersions. With SOC, a Dirac gap of $2E_g$ is opened and the maximum of the hole band, defined here as ε_F, is formed above the theoretical Fermi level E_F. The optical gap (red double arrow) is then estimated as $2(E_g + \varepsilon_F)$. The upper inset shows the optical conductivity of $Ni_3In_2S_2$ at 10 K, with the Drude background subtracted to reveal the linearly increasing optical gap at 45 ± 3 meV. The lower inset shows the endless Dirac nodal lines obtained by DFT calculations and Berry phase of π from charge carriers orbiting a loop enclosing a node.

expressed as

$$E_n = \pm\sqrt{2e\hbar n\mu_0 H v_F^2 + E_g^2}, \tag{2}$$

where v_F is the Fermi velocity and E_g is half of the energy gap between the minimum and maximum points of the electron (+) and holelike (−) Dirac bands. The lth Landau level (with integer l) reaches the Fermi level (E_F) by tuning the magnetic field H, so that $E_{n=l}$ corresponds to the energy difference between the Dirac point and E_F. This results in a surge in carrier density near E_F, leading to peaks in the free energy f, which manifest as quantum oscillations. For the magnetization, however, $M = -(\frac{\partial f}{\partial H})_T$ introduces a phase shift of $\pi/2$ in inverse field, meaning that H satisfying $E_{n=l-1/4}$ (not $E_{n=l}$) to be the energy difference should be the local maxima in dHvA oscillations. To assign Landau level indices to the oscillation minima and maxima of F_α, dHvA oscillations in inverse field are shown in Fig. 4(c). The gray and magenta curves represent background-subtracted sub-Kelvin torque and its low-pass filtered data at $\theta = -10^\circ$, respectively, while the violet curve shows smoothed ΔM data from VSM at 2 K to suppress oscillations originating from other pockets.

In the two F_α curves in Fig. 4(c), local maxima and minima (dashed lines) are assigned as $l - 1/4$ and $l + 1/4$ points, respectively, and plotted on the Landau fan diagram in Fig. 4(d). From the quasi-2D nature of the hole band as shown in Figs. 3(d) and 3(e), the Berry phase ϕ_B can be determined using the relation $n_0 = 1/2 - \phi_B/2\pi$ [35]. Both extrapolation results show a nonzero ϕ_B close to π consistent with predictions from Dirac nodes as outlined in Ref. [14]. This observation aligns with the simulated and experimental oscillations supporting the nontrivial topology of the system (Fig. S4(b) [26]). The inset of Fig. 4(d) shows a transition from quadratic to linear MR occurring around 12.7 T, closely corresponding to the magnetic field required to reach $n = 1$, which will be discussed further later. Additionally, it is noteworthy that an $n = 0.75$ peak is observed at $\mu_0 H \approx 17$ T, representing the last local maximum in the dHvA oscillations of F_α. This peak remains unsplit, possibly due to a small Landé g factor.

Figure 4(e) presents the zoomed-in view of the band structure of $Ni_3In_2S_2$ near B1, where the red (dark-cyan) curve represents massive (massless) Dirac bands with (without) SOC. When the maximum point of the massive hole band is defined as ε_F relative to the nominal Fermi level E_F, the theoretically calculated value is $\varepsilon_F \approx 3$ meV. The center of the Dirac gap, associated with the Dirac node forming the endless Dirac nodal lines [14] in the absence of SOC (lower inset, Fig. S10 [26]), is located at $E_g \approx 24$ meV above ε_F. This finite gap may account for the small deviation of the Berry phase from π in Fig. 4(d) [36]. Interestingly, the Dirac nodes of $Ni_3In_2S_2$ are predicted to be located closer to E_F than those of its ferromagnetic sister compound $Co_3Sn_2S_2$, where the Weyl nodes are positioned $50-60$ meV above E_F. In $Co_3Sn_2S_2$, Weyl nodes are known to generate the large Berry curvature responsible for the intrinsic anomalous Hall effect [17,37]. For $Ni_3In_2S_2$, the presence of nodal lines can be probed by detecting a nonzero Berry phase, which arises from charge carriers traversing a closed orbit that encloses the nodal lines and, in this case, corresponds to the cyclotron orbit α [Fig. 4(d)].

Interestingly, an optical band gap of $2(E_g+\varepsilon_F) \approx 54$ meV, originating from interband transitions between the Dirac bands, can be predicted based on the selection rule [38]. The optical band gap of Dirac bands can be detected through the linear increase in optical conductivity at low photon energy (Fig. S8 [26]). The upper inset of Fig. 4(e) shows such optical conductivity data after subtraction of the Drude peak, exhibiting an almost linearly increasing behavior starting from 45 meV, which closely matches the DFT prediction of 54 meV. The linear behavior and the small gapped structure are consistent with observations in previously studied nodal-line semimetals [39,40]. The energy dispersion for the quasi-2D massive Dirac fermions near B1 is given by

$$E(k)-E_F = E_g+\varepsilon_F \pm \sqrt{E_g^2+(\hbar k v_F)^2},$$
$$\text{where } v_F = \sqrt{2e\hbar F_\alpha}/m_\alpha^*. \tag{3}$$

From Eq. (3), at $k=k_F$, we get $E_g+\varepsilon_F = \sqrt{(E_g)^2+(\hbar k_F v_F)^2}$ for the hole band. Applying $2(E_g+\varepsilon_F) \approx 45$ meV, $F_\alpha \approx 10$ T, and $m_\alpha^* \approx 0.183 m_0$ from experimental data, we obtain $\varepsilon_F \approx 3.9$ meV and $E_g \approx 18.6$ meV, again demonstrating a qualitatively good agreement between the simulation and the measurement.

Based on the torque and VSM results, we analyzed the temperature and field dependence of oscillation amplitudes for each orbit to extract the physical parameters summarized in Table I. The Fermi wave vector was determined by the Onsager relation, $k_F = \sqrt{2eF/\hbar}$, while the effective mass m^* and Dingle temperature T_D were obtained by fitting the LK formula [27]. From these results, quantum scattering time $\tau_s = \hbar/(2\pi k_B T_D)$ and quantum mobility $\mu = e\tau_s/m^*$ were derived (Figs. S7 and S9 [26]). Note that the parameters presented in Table I provide complete quantitative determination of the quantum mobilities for all fundamental orbits of $Ni_3In_2S_2$; previously, only the quantum mobility for the orbit α ($1.1\ m^2\,V^{-1}\,S^{-1}$) was reported by Zhang *et al.* [16]. According to Table I, the massive Dirac fermions on the orbit α exhibit μ of $0.88\ m^2\,V^{-1}\,S^{-1}$, a value comparable to the previous report. More importantly, the quantum mobility of the orbit α demonstrates an order of magnitude higher than the others. This suggests that despite its small carrier density expected from a low oscillation frequency, the α pocket could still significantly contribute to electrical transport. Therefore, we propose that the massive Dirac fermions observed in the dHvA oscillations play an important role in the origin of the nonsaturating giant MR of $Ni_3In_2S_2$.

The scenario of the carrier-compensated semimetal based on the two-carrier model, as used by Fang *et al.* [15], may explain large quadratic MR observed at low field regions below 12 T. As shown in the inset of Fig. 4(d), the field derivative of MR increases linearly up to 12 T, indicating quadratic MR and qualitatively supporting the two-carrier model. However, the two-carrier model also suggests saturation of quadratic MR at high fields, as perfect compensation is unrealistic in real materials, typically containing more than two different carrier pockets. Contrarily, the field derivative in the inset of Fig. 4(d) becomes nearly constant above 12.7 T and up to 31 T (Fig. S2 [26]). As a result, the MR in Fig. 1(d) continues to increase approximately linearly up to 31 T. The unusual, nonsaturating MR behavior extends beyond the model of the compensated semimetal and aligns with Zhang *et al.*'s observations, which reported unsatisfactory fits of the two-carrier model to longitudinal and Hall resistivity data between 11 and 14 T [16]. Therefore, the nonsaturating linear MR behavior found above 12 T in $Ni_3In_2S_2$ cannot be solely explained by the carrier-compensation model.

To uncover the origin of nonsaturating MR, we propose that the quantum limit of the orbit α must be considered. In Fig. 4(d), the first Landau level crosses the Fermi level at $1/\mu_0 H \approx 0.083\ T^{-1}$, or $\mu_0 H \approx 12$ T, just before the onset of linear MR. At this field and above, Dirac fermions are concentrated in the zeroth Landau level, fulfilling the theoretical condition for the linear quantum MR [41–43]. While carrier compensation within the two-carrier model may play a role at lower fields, its influence is likely limited to this regime. At higher magnetic fields, the linear MR becomes dominated by the quantum behavior of electrons in the zeroth Landau level. The nonsaturating linear MR observed in $Ni_3In_2S_2$ also provides valuable insights into similar phenomena in the sister semimetal, $Co_3Sn_2S_2$, which hosts Weyl nodes due to time-reversal symmetry breaking. While the linear MR in $Co_3Sn_2S_2$ has been discussed in association with the quantum limit and Dirac states at high fields [44], its origin still remains under debate [17,45,46]. The observed quadratic-to-linear MR crossover in $Ni_3In_2S_2$ underscores the pivotal role of massive Dirac fermions reaching their first Landau level in shaping the electrical transport behavior. This finding may also offer a pathway to understanding analogous phenomena across the broader 322-kagome family.

IV. CONCLUSIONS

In this study, we report quantum oscillations of the kagome semimetal $Ni_3In_2S_2$ under high magnetic fields up to 31 T. Angle-dependent torque magnetometry revealed the presence

of a quasi-2D hole band and 3D electron bands, consistent with DFT calculations. Tunneling orbits were observed for the angle $\theta \leqslant 65°$ between the c-axis and magnetic field directions, indicating small separations between cyclotron orbits in momentum space, consistent with the nodal-line semimetal framework. Notably, charge carriers on the smallest orbit of $F_\alpha \approx 10$ T, which encloses an endless Dirac nodal line, exhibited a small effective mass of $0.183m_0$ and Berry phase close to π. This suggests that they are topologically nontrivial, massive Dirac fermions having a small gap induced by SOC. Infrared spectroscopy supported these findings by revealing a linear increase in optical conductivity above a photon energy of 45 meV, corresponding to the small optical band gap opened by SOC. Additionally, the Dirac fermions demonstrated an order of magnitude higher quantum mobility compared to other bands with heavier charge carriers. This high mobility likely contributes to the nonsaturating linear MR observed above 12.7 T, where the Dirac fermions are concentrated on a single Landau level, evidenced by dHvA oscillations results. These findings position $Ni_3In_2S_2$ as a compelling kagome nodal-line semimetal that hosts Dirac fermions responsible for the quantum MR, making it a promising platform for exploring rich physics, including anomalous Hall effects [9,12,17,47] and Klein tunneling [29,31].

ACKNOWLEDGMENTS

The work at SNU was supported by the Ministry of Science and ICT through National Research Foundation of Korea (Grants No. 2022H1D3A3A01077468 and No. RS-2024–00338707) and by the Ministry of Education through the core facility program (Grant No. 2021R1A6C101B418). The work at HYU was supported by the National Research Foundation of Korea funded by the Ministry of Science and ICT (Grants No. 2022R1F1A1072865 and No. RS-2024–00416036). W.K. was supported by the National Research Foundation of Korea (Grant No. 2018R1A6A1A03025340). Experiments performed at the National High Magnetic Field Laboratory were supported by National Science Foundation Cooperative Agreement No. DMR-2128556 and the State of Florida.

DATA AVAILABILITY

The data that support the findings of this article are not publicly available upon publication because it is not technically feasible and/or the cost of preparing, depositing, and hosting the data would be prohibitive within the terms of this research project. The data are available from the authors upon reasonable request.

[1] S. Sachdev, Kagome-and triangular-lattice Heisenberg antiferromagnets: Ordering from quantum fluctuations and quantum-disordered ground states with unconfined bosonic spinons, Phys. Rev. B **45**, 12377 (1992).

[2] W. S. Wang, Z. Z. Li, Y. Y. Xiang, and Q. H. Wang, Competing electronic orders on kagome lattices at van Hove filling, Phys. Rev. B **87**, 115135 (2013).

[3] K. Y. Chen, N. N. Wang, Q. W. Yin, Y. H. Gu, K. Jiang, Z. J. Tu, C. S. Gong, Y. Uwatoko, J. P. Sun, H. C. Lei, J. P. Hu, and J.-G. Cheng, Double superconducting dome and triple enhancement of T_c in the kagome superconductor CsV_3Sb_5 under high pressure, Phys. Rev. Lett. **126**, 247001 (2021).

[4] Y. Sur, K. T. Kim, S. Kim, and K. H. Kim, Optimized superconductivity in the vicinity of a nematic quantum critical point in the kagome superconductor $Cs(V_{1-x}Ti_x)_3Sb_5$, Nat. Commun. **14**, 3899 (2023).

[5] Y. M. Oey, B. R. Ortiz, F. Kaboudvand, J. Frassineti, E. Garcia, R. Cong, S. Sanna, V. F. Mitrović, R. Seshadri, and S. D. Wilson, Fermi level tuning and double-dome superconductivity in the kagome metal $CsV_3Sb_{5-x}Sn_x$, Phys. Rev. Mater. **6**, L041801 (2022).

[6] D. H. Gim, D. Wulferding, C. Lee, H. Cui, K. Nam, M. J. Han, and K. H. Kim, Fingerprints for anisotropic Kondo lattice behavior in the quasiparticle dynamics of the kagome metal Ni_3In, Phys. Rev. B **108**, 115143 (2023).

[7] L. Ye, S. Fang, M. Kang, J. Kaufmann, Y. Lee, C. John, P. M. Neves, S. Y. Frank Zhao, J. Denlinger, C. Jozwiak, A. Bostwick, E. Rotenberg, E. Kaxiras, D. C. Bell, O. Janson, R. Comin, and J. G. Checkelsky, Hopping frustration-induced flat band and strange metallicity in a kagome metal, Nat. Phys. **20**, 610 (2024).

[8] D. Di Sante, C. Bigi, P. Eck, S. Enzner, A. Consiglio, G. Pokharel, P. Carrara, P. Orgiani, V. Polewczyk, J. Fujii, P. D. C. King, I. Vobornik, G. Rossi, I. Zeljkovic, S. D. Wilson, R. Thomale, G. Sangiovanni, G. Panaccione, and F. Mazzola, Flat band separation and robust spin Berry curvature in bilayer kagome metals, Nat. Phys. **19**, 1135 (2023).

[9] L. Ye, M. Kang, J. Liu, F. von Cube, C. R. Wicker, T. Suzuki, C. Jozwiak, A. Bostwick, E. Rotenberg, D. C. Bell, L. Fu, R. Comin, and J. G. Checkelsky, Massive Dirac fermions in a ferromagnetic kagome metal, Nature (London) **555**, 638 (2018).

[10] Z. Song, T. Zhang, and C. Fang, Diagnosis for nonmagnetic topological semimetals in the absence of spin-orbital coupling, Phys. Rev. X **8**, 031069 (2018).

[11] Z. Ren, A. A. Taskin, S. Sasaki, K. Segawa, and Y. Ando, Fermi level tuning and a large activation gap achieved in the topological insulator Bi_2Te_2Se by Sn doping, Phys. Rev. B **85**, 155301 (2012).

[12] Z. Hao, Y. Cai, Y. Liu, Y. Wang, X. Sui, X.-M. Ma, Z. Shen, Z. Jiang, Y. Yang, W. Liu, Q. Jiang, Z. Liu, M. Ye, D. Shen, Y. Liu, S. Cui, J. Chen, L. Wang, C. Liu, J. Lin *et al.*, Dirac nodal lines and nodal loops in the topological kagome superconductor CsV_3Sb_5, Phys. Rev. B **106**, L081101 (2022).

[13] R. Chapai, M. Leroux, V. Oliviero, D. Vignolles, N. Bruyant, M. P. Smylie, D. Y. Chung, M. G. Kanatzidis, W.-K. Kwok, J. F. Mitchell, and U. Welp, Magnetic breakdown and topology in the kagome superconductor CsV_3Sb_5 under high magnetic field, Phys. Rev. Lett. **130**, 126401 (2023).

[14] T. Zhang, T. Yilmaz, E. Vescovo, H. X. Li, R. G. Moore, H. N. Lee, H. Miao, S. Murakami, and M. A. McGuire, Endless Dirac nodal lines in kagome-metal $Ni_3In_2S_2$, npj Comput. Mater. **8**, 155 (2022).

[15] H. Fang, M. Lyu, H. Su, J. Yuan, Y. Li, L. Xu, S. Liu, L. Wei, X. Liu, H. Yang, Q. Yao, M. Wang, Y. Guo, W. Shi, Y. Chen, E. Liu, and Z. Liu, Record-high mobility and extreme magnetoresistance on kagome-lattice in compensated semimetal $Ni_3In_2S_2$, Sci. China Mater. **66**, 2032 (2023).

[16] Y. Zhang, Z. Li, K. W. Chen, L. Li, and C. Uher, Extremely large magnetoresistance and quantum oscillations in semimetal $Ni_3In_2S_2$, Mater. Today Phys. **40**, 101318 (2024).

[17] E. Liu, Y. Sun, N. Kumar, L. Muechler, A. Sun, L. Jiao, S.-Y. Yang, D. Liu, A. Liang, Q. Xu, J. Kroder, V. Süß, H. Borrmann, C. Shekhar, Z. Wang, C. Xi, W. Wang, W. Schnelle, S. Wirth, Y. Chen *et al.*, Giant anomalous Hall effect in a ferromagnetic kagome-lattice semimetal, Nat. Phys. **14**, 1125 (2018).

[18] P. Hohenberg and W. Kohn, Inhomogeneous electron gas, Phys. Rev. **136**, B864 (1964).

[19] P. Giannozzi, S. Baroni, N. Bonini, M. Calandra, R. Car, C. Cavazzoni, D. Ceresoli, G. L. Chiarotti, M. Cococcioni, and I. Dabo, QUANTUM ESPRESSO: A modular and open-source software project for quantum simulations of materials, J. Phys.: Condens. Matter **21**, 395502 (2009).

[20] P. E. Blöchl, Projector augmented-wave method, Phys. Rev. B **50**, 17953 (1994).

[21] J. P. Perdew, K. Burke, and M. Ernzerhof, Generalized gradient approximation made simple, Phys. Rev. Lett. **77**, 3865 (1996).

[22] M. Kawamura, FermiSurfer: Fermi-surface viewer providing multiple representation schemes, Comput. Phys. Commun. **239**, 197 (2019).

[23] M. I. Katsnelson, K. S. Novoselov, and A. K. Geim, Chiral tunnelling and the Klein paradox in graphene, Nat. Phys. **2**, 620 (2006).

[24] F. D. M. Haldane, Model for a quantum Hall effect without Landau levels: Condensed-matter realization of the "parity anomaly", Phys. Rev. Lett. **61**, 2015 (1988).

[25] H. Zhang, Q. Li, M. G. Scheer, R. Wang, C. Tuo, N. Zou, W. Chen, J. Li, X. Cai, C. Bao, M.-R. Li, K. Deng, K. Watanabe, T. Taniguchi, M. Ye, P. Tang, Y. Xu, P. Yu, J. Avila, P. Dudin *et al.*, Correlated topological flat bands in rhombohedral graphite, Proc. Natl. Acad. Sci. USA **121**, e2410714121 (2024).

[26] See Supplemental Material at http://link.aps.org/supplemental/10.1103/6jzx-mdjv for details of sample alignment, additional data for field-induced tunneling, LK formula fitting, and infrared spectroscopy.

[27] D. Shoenberg, *Magnetic Oscillations in Metals* (Cambridge University Press, Cambridge, 1984).

[28] E. I. Blount, Bloch electrons in a magnetic field, Phys. Rev. **126**, 1636 (1962).

[29] T. E. O'Brien, M. Diez, and C. W. J. Beenakker, Magnetic breakdown and Klein tunneling in a type-II Weyl semimetal, Phys. Rev. Lett. **116**, 236401 (2016).

[30] S. Pezzini, M. R. van Delft, L. M. Schoop, B. V. Lotsch, A. Carrington, M. I. Katsnelson, N. E. Hussey, and S. Wiedmann, Unconventional mass enhancement around the Dirac nodal loop in ZrSiS, Nat. Phys. **14**, 178 (2018).

[31] M. R. van Delft, S. Pezzini, T. Khouri, C. S. A. Müller, M. Breitkreiz, L. M. Schoop, A. Carrington, N. E. Hussey, and S. Wiedmann, Electron-hole tunneling revealed by quantum oscillations in the nodal-line semimetal HfSiS, Phys. Rev. Lett. **121**, 256602 (2018).

[32] J. Hu, Z. Tang, J. Liu, X. Liu, Y. Zhu, D. Graf, K. Myhro, S. Tran, C. N. Lau, J. Wei, and Z. Mao, Evidence of topological nodal-line fermions in ZrSiSe and ZrSiTe, Phys. Rev. Lett. **117**, 016602 (2016).

[33] P. Leng, N. B. Joseph, X. Cao, Y. Qian, Z. Li, Q. Ma, L. Ai, A. Banerjee, Y. Zhang, Z. Jia, Y. Zhang, C. Xi, L. Pi, A. Narayan, J. Zhang, and F. Xiu, Thickness-dependent magnetic breakdown in ZrSiSe nanoplates, Nano Lett. **24**, 5125 (2024).

[34] H. Kim, J. M. Ok, S. Cha, B. G. Jang, C. I. Kwon, Y. Kohama, K. Kindo, W. J. Cho, E. S. Choi, Y. J. Jo, W. Kang, J. H. Shim, K. S. Kim, and J. S. Kim, Quantum transport evidence of isolated topological nodal-line fermions, Nat. Commun. **13**, 7188 (2022).

[35] G. P. Mikitik and Yu. V. Sharlai, Manifestation of Berry's phase in metal physics, Phys. Rev. Lett. **82**, 2147 (1999).

[36] H. Z. Lu, J. Shi, and S. Q. Shen, Competition between weak localization and antilocalization in topological surface states, Phys. Rev. Lett. **107**, 076801 (2011).

[37] Q. Wang, Y. Xu, R. Lou, Z. Liu, M. Li, Y. Huang, D. Shen, H. Weng, S. Wang, and H. Lei, Large intrinsic anomalous Hall effect in half-metallic ferromagnet $Co_3Sn_2S_2$ with magnetic Weyl fermions, Nat. Commun. **9**, 3681 (2018).

[38] B. Xu, Y. M. Dai, L. X. Zhao, K. Wang, R. Yang, W. Zhang, J. Y. Liu, H. Xiao, G. F. Chen, A. J. Taylor, D. A. Yarotski, R. P. Prasankumar, and X. G. Qiu, Optical spectroscopy of the Weyl semimetal TaAs, Phys. Rev. B **93**, 121110(R) (2016).

[39] Y. M. Shao, Z. Y. Sun, Y. Wang, C. C. Xu, R. Sankar, A. J. Breindel, C. Cao, M. M. Fogler, F. C. Chou, Z. Q. Li, T. Timusk, M. B. Maple, and D. N. Basov, Optical signatures of Dirac nodal lines in $NbAs_2$, Proc. Natl. Acad. Sci. USA **116**, 1168 (2019).

[40] R. Yang, T. Zhang, L. Zhou, Y. Dai, Z. Liao, H. Weng, and X. Qiu, Magnetization-induced band shift in ferromagnetic Weyl semimetal $Co_3Sn_2S_2$, Phys. Rev. Lett. **124**, 077403 (2020).

[41] A. A. Abrikosov, Quantum magnetoresistance, Phys. Rev. B **58**, 2788 (1998).

[42] Y. Zhou, H. Wu, D. Yu, and Z. Liao, Magnetoresistance in graphene under quantum limit regime, Appl. Phys. Lett. **102**, 093116 (2013).

[43] J. Hu and T. F. Rosenbaum, Classical and quantum routes to linear magnetoresistance, Nat. Mater. **7**, 697 (2008).

[44] V. Nagpal and S. Patnaik, Breakdown of Ohm's law and nontrivial Berry phase in magnetic Weyl semimetal $Co_3Sn_2S_2$, J. Phys.: Condens. Matter **32**, 405602 (2020).

[45] M. Tanaka, Y. Fujishiro, M. Mogi, Y. Kaneko, T. Yokosawa, N. Kanazawa, S. Minami, T. Koretsune, R. Arita, S. Tarucha, M. Yamamoto, and Y. Tokura, Topological kagome magnet $Co_3Sn_2S_2$ thin flakes with high electron mobility and large anomalous Hall effect, Nano Lett. **20**, 7476 (2020).

[46] J. Zhao, B. Jiang, S. Zhang, L. Wang, E. Liu, Z. Li, and X. Wu, Magnetoresistance signature of two-dimensional electronic states in $Co_3Sn_2S_2$, Phys. Rev. B **107**, 085203 (2023).

[47] N. A. Sinitsyn, A. H. MacDonald, T. Jungwirth, V. K. Dugaev, and J. Sinova, Anomalous Hall effect in a two-dimensional Dirac band: The link between the Kubo-Streda formula and the semiclassical Boltzmann equation approach, Phys. Rev. B **75**, 045315 (2007).